Towards a Mechanistic Understanding of Pellet Cladding Interaction using advanced 3D Characterisation and Atomistic Simulation

Philipp Frankel[1]*, Alistair Garner[1], Adam Plowman[1], Sean Hanlon[2], Conor Gillen[1], Andrew Phillion[2], Christopher P. Race[1], Jack Donoghue[1], Clara Anghel[4], Antoine Ambarde[5], Mark Daymond[3],

[1] School of Materials, The University of Manchester, Manchester M13 9PL, UK
[2] Canadian Nuclear Laboratories, 286 Plant Road, Chalk River, ON, K0J 1J0, Canada
[3] Department of Mechanical and Materials Engineering, Queen's University, Kingston, Ontario K7L 3N6, Canada
[4] Westinghouse Electric Sweden AB, Västerås, Sweden
[5] EDF Research and Development, Materials and Mechanics of Components, Ecuelles, 77818 Moret-sur-Loing, France

Abstract

Iodine induced stress corrosion cracking (I-SCC) has long been proposed as a primary cause of pellet cladding interaction (PCI) failures in light water reactors. The I-SCC process has been studied in great detail but its precise mechanism and the influence of local microstructure remains uncertain. We performed a large scale investigation of a sample produced by a novel rig for I-SCC using analytical 3D characterisation and relate this to atomistic simulations describing the orientation dependence of iodine segregation and its influence on various types of boundaries. In situ monitoring capability enabled an I-SCC crack to be arrested in a CT specimen machined from Zr-4 plate before failure and serial sectioning by plasma-FIB allowed detailed characterization of an entire cracked region consisting of nearly 1000 grains. By relating the crack path to the local microstructure in 3D, new insights can be gained about the crack propagation during I-SCC. The crack is observed to be primarily transgranular in nature, progressing along basal planes, but away from the crack tip a significant proportion of intergranular cracking was also observed. By careful analysis we are able to relate the nature of the crack progression directly to the individual grain orientations and their level of deformation. Particular grain orientations are observed to be resistant to I-SCC attack and result in crack deflection. The formation of twins in the vicinity of the crack are also observed and their role is discussed. Complementary density functional theory (DFT) modelling has examined the effects of iodine impurities at different positions within the microstructure. Simulations suggested that TG basal cleavage is energetically accessible and may be preferable to cleavage on prismatic planes, even if this would result in significant deviation of the crack path. These results are discussed with respect to the experimental observations.

Introduction

Pellet cladding interaction (PCI) is a light water reactor fuel failure phenomenon widely attributed to iodine-induced stress corrosion cracking (I-SCC) [1,2]. Although studied extensively when PCI failures were first discovered in the 1960s, research in recent years has declined due to the introduction of a number of effective but over conservative mitigation measures that have led to significant reductions in the number of PCI failures in the past two decades [3]. However, modern reactors are required to be more reactive due to increased production of energy from renewable sources and therefore there is increasing need for better understanding of the underlying mechanisms of I-SCC to reduce the reliance on

conservative operational restrictions for safe reactor operation. Boiling water reactors (BWR), which are more susceptible to PCI failures due to control rod reactivity management, now exclusively contain lined zirconium cladding [2] and power ramp speed and magnitudes are severely limited to maintain the stress on the inner surface of the cladding below empirically derived thresholds [4]. One particular operating regime referred to as extended reduced power operation (ERPO) significantly increases the likelihood of PCI failures due to build up of iodine and rapid fuel expansion during subsequent power ramp, with the situation compounded by fission gas swelling [5,6].

The generally accepted current understanding of the I-SCC process is that volatile fission products, the most likely of which is iodine (although others have not been ruled out), firstly penetrate the protective oxide. Iodine penetration is most likely to occur through cracks in the oxide, as the brittle oxide fractures at relatively low hoop stresses [7]. When the bare metal is exposed to iodine, a number of different mechanisms have been proposed for both crack initiation and propagation [REFS]. It is generally agreed that crack initiation occurs at zirconium grain boundaries (GBs), with the formation of a number of zirconium iodide compounds until the volatile ZrI_4 compound is formed, which can actively remove Zr atoms and lead to GB pitting. Although this mechanism has been theoretically examined [7], experimental evidence is lacking. Park et al. however provided evidence of zirconium iodide-containing pits preferentially forming at GBs [8] and more recently, Gillen et al. showed evidence of iodine segregation ahead of a crack tip in irradiated material, which was believed to be zirconium iodide formation at a GB ahead of the crack tip [9]. The exact role of iodine in crack propagation is also not well understood, although evidence suggests that the surface mobility mechanism which has previously been suggested as a likely contributing factor in other cases of SCC [10], could be responsible for I-SCC propagation [11–13].

Cracking is known to progress at comparatively low crack tip stress intensities intergranularly, until the crack grows large enough that the high stress intensity produces transgranular cracking, with material overload eventually occurring [1,2,8,12] .Transgranular cracking is typically observed to occur through pseudo-cleavage exclusively of the basal plane of the HCP structured zirconium matrix [1,14–18], although the situation becomes less clear following irradiation [9]. Ab initio modelling has shown that iodine adsorption onto zirconium can reduce the Gibbs free surface energy, preferentially affecting the basal plane and thus promoting cleavage of those planes [19]. Localised ductile tearing, referred to as prismatic fluting, is thought to allow for crack propagation between unaligned basal planes resulting in characteristic patterns on fracture surfaces [20]. This combination of basal cleavage and prismatic fluting is commonly referred to as pseudo-cleavage [1]. Any observations of this phenomenon has so far been limited to small scale 2-dimensional analysis providing limited statistics [16,18] or fractographic analysis from which it is very difficult to relate back to local crystallographic orientation.

In this work, we aim to shed some light on I-SCC propagation mechanisms through large scale 3D characterisation and relate this to atomistic simulations describing the orientation dependence of iodine segregation. A novel rig for I-SCC testing has been developed which allows for control of iodine partial pressures with in situ monitoring capability and for the testing of a number of different sample geometries under different loading regimes. For this study, a test was stopped prior to failure allowing for an entire cracked region to be lifted out using a plasma-FIB and subject to serial sectioning analysis. This allowed

us to reconstruct the microstructure and crack morphology in 3D which not only allows for a statistical analysis of I-SCC propagation but allows us to explore the third dimension and how this affects our understanding of I-SCC. This is complemented by a systematic modelling study using density functional theory (DFT) that has examined the effects of iodine impurities on grain boundary properties.

Materials and methods

Materials selection and testing

Compact tension (CT) specimens were machined from 1.3" thick recrystallised Zr-4 plate material supplied by ATI Wah Chang with an averaged equiaxed grain diameter of 10 μm. As these samples were tested during the commissioning stage of the experimental rig, they were machined to allow testing in the most susceptible geometry, i.e. with the loading direction parallel to the plate normal direction and thus perpendicular to the majority of the basal planes. In the following analyses, the major tensile axis is assumed to be the X-direction and crack propagation is in the Z direction. A schematic of the testing rig developed at Canadian Nuclear Laboratories (CNL) is presented in Figure 1. The entire rig is contained within a walk-in fume hood in an active laboratory and full details of the experimental set up can be found in ref [21]. Argon is used as carrier gas and pure solid iodine is heated in the first heat bath, with the partial pressure controlled by the heat bath temperature and a second heat bath is maintained at a slightly lower temperature to ensure the vapour phase is at or near equilibrium. The lines after the second heat bath are heated to ensure no iodine precipitation occurs in the glass lines until after the gas leaves the oven. The load train is made of iodine-resistant Hastelloy alloy C276. The rig is fitted with a reversing direct current potential drop (DCPD) system in order to detect crack initiation and monitor crack growth, more details of the DCPD system can also be found in ref [21]. The rig allows for independent control of specimen temperature, iodine partial pressure and the loading regime with in situ measurement of crack initiation and growth. For this test, the first and second heat bath temperatures were set at 55 C and 50 C, respectively, corresponding to an iodine partial pressure of 293 Pa in the specimen chamber. After the DCPD leads were spotwelded and the chamber assembled, Ar gas was used to purge the chamber at room temperature with a flow rate of 100 ccm, which was reduced to 20 ccm before prefatiguing began. No iodine was present in the specimen chamber at this point; the Ar cover gas bypassed the iodine flask. After prefatiguing, the gas flow was diverted to allow for iodine to enter the specimen chamber and the sample held at constant load at 3800 N (K=20 MPa$\sqrt{m}$) until the test was stopped. The resulting DCPD curve is shown in Figure 4 and a full description is provided in the results section. The crack grew a total of ~ 5.2 mm before the test was terminated. The specimen was cut half in the thickness direction, then half of the crack was opened to expose the fracture surface. The other intact half was then shipped to the University of Manchester for 3D-EBSD examination.

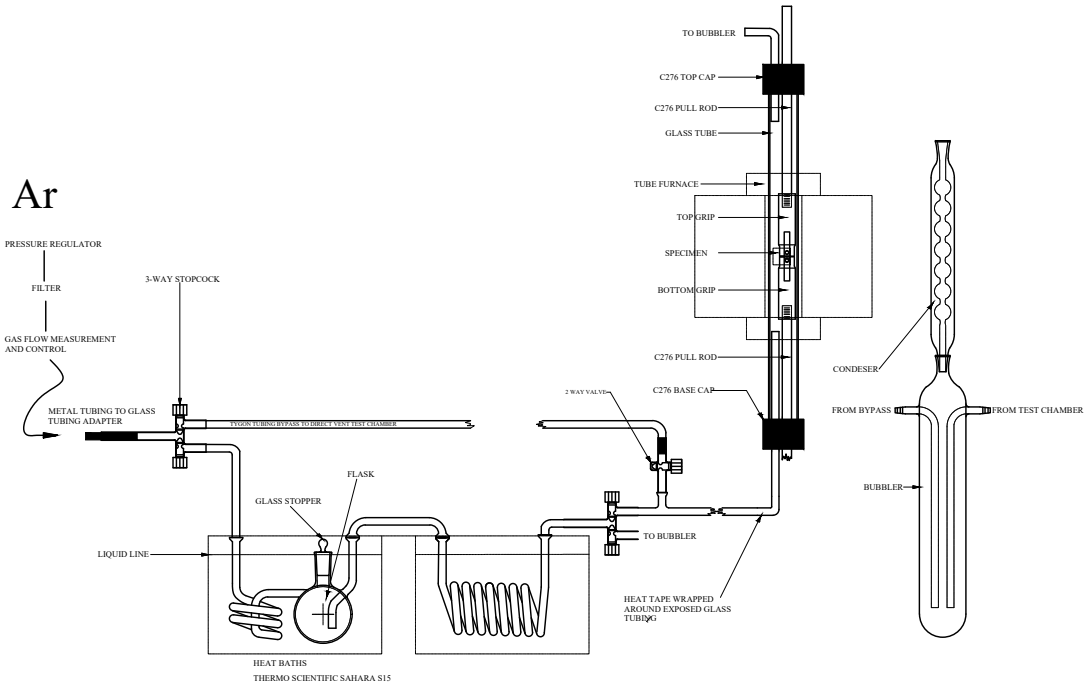

Figure 1: Schematic of the experimental set up for I-SCC testing at CNL

Serial sectioning using plasma focused ion beam

The sample from the test terminated prior to failure was firstly polished using standard metallographic procedures from the normal direction of the CT specimen in order to reveal the fine details of the crack path. The region of interest (ROI) was selected to attempt to capture as much of the crack tip region as possible in the final volume, as the subsurface crack morphology was not known. After protecting the ROI, the volume was lifted out and attached to a Cu grid using an FEI Helios Xe^+ plasma focused ion beam (P-FIB) according to the procedure outlined in ref. [22]. The final block dimensions were approximately 80 x 120 x 200 μm. The serial sectioning experiment was performed using FEI Auto slice and view 4 software using the FEI Helios PFIB using a 30 kV ion beam operated at 180 nA and a 30 kV electron beam operated at 22 nA. The slice thickness was 300 nm and a rocking mill of 5° was used to reduce curtaining effects [23]. After each slice, electron backscatter diffraction (EBSD) and electron dispersive X-ray spectroscopy (EDX) maps were collected automatically over an area of approximately 100 x 100 μm with a step size of 300 nm using AZTEC software from Oxford Instruments. In total 485 slices were collected, giving a total analysed volume of 1.5 x 10^6 μm^3. In addition, after each slice, a forescatter detector (FSD) image was collected using FSD diodes integrated with the Oxford Instruments Nordlys EBSD detector in order to image the crack path. Images were 4096 x 2560 resolution with a dwell time of 3 μs. These images were found to give improved contrast to standard secondary electron images to enable segmentation of the crack path in subsequent processing stages

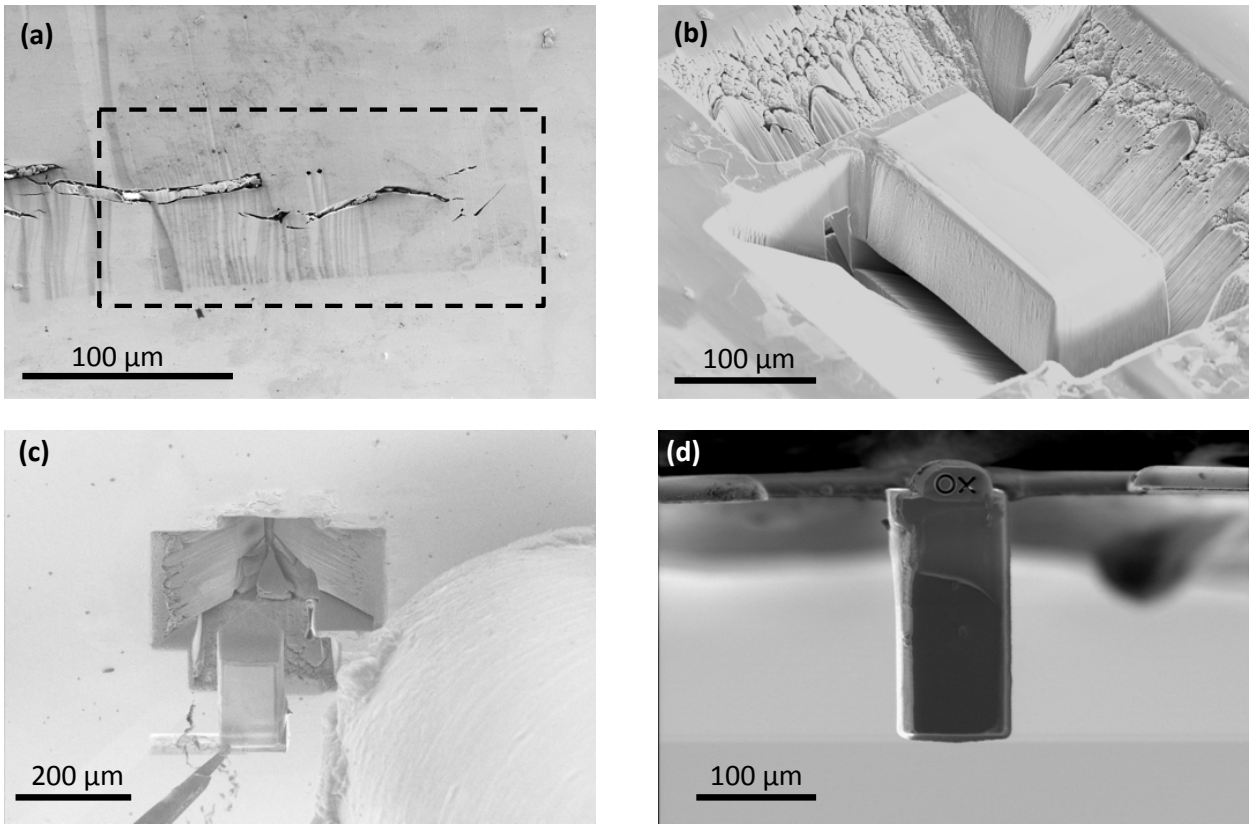

Figure 2: (a) and (b) Secondary electron images showing crack tip and trench digging around region of interest for liftout, (c) and (d) ion beam images showing liftout procedure using micromanipulator and final volume attached to Cu post with ion milled fiducial marker

Data analysis and reconstruction

Processing and reconstruction of EBSD data was performed using Dream.3D software [24]. The initial EBSD data was firstly cleaned, aligned and segmented in 3 dimensions according to a critical misorientation tolerance of 3°. After segmentation, intragranular misorientation was calculated in each grain using Dream.3D and a surface mesh was applied the grains to the voxelised grain surfaces to aid with visualisation and subsequent grain boundary calculations. Initial processing of the FSD images was performed using ImageJ. The images were firstly filtered, aligned and a binary threshold was applied in order to segment the crack from the bulk material. After preprocessing, the aligned images were loaded into Dream.3D and further fine alignment was performed. The aligned images were then segmented in 3D according to scalar tolerance of 1 and a surface mesh was again applied. of all 3D data was achieved using Paraview. After reconstruction of both datasets, they were transformed manually using Paraview in order to align the crack path with the remaining non-indexed points from the EBSD measurement. Orientation analysis was performed using Oxford Instruments Channel 5 software.

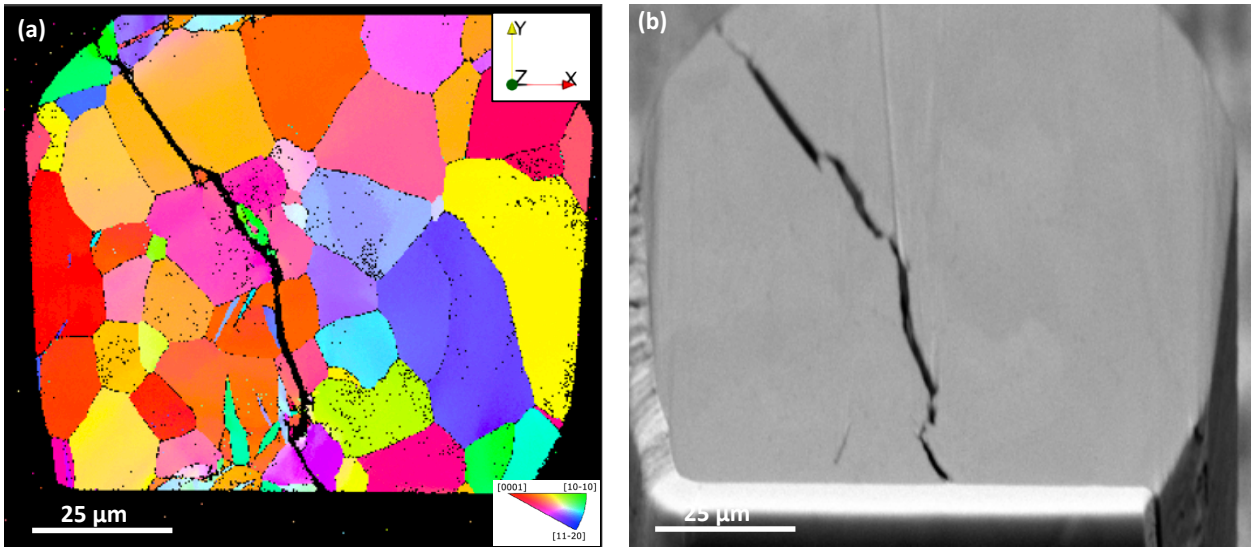

Figure 3: Typical images from serial sectioning used for 3D reconstruction (a) EBSD orientation map in IPF-X colouring and (b) corresponding FSD image showing detailed crack path.

Density functional theory

To complement the experimental analysis, and to gain insight into the crack path observations, we also performed first-principles simulations on the energetics of various interfaces in Zr, using density functional theory (DFT) [25,26]. We employed the plane wave, pseudopotential DFT code CASTEP [27] (version 17.2) to find the optimised configurations and energies of a set of low-Σ grain boundaries (GBs). In particular, we studied four symmetric tilt grain boundaries (STGBs) about the $[0001]$ axis, with Σ-values, GB planes and misorientation angles given by: $\Sigma7(1\bar{3}20)$ 21.79°, $\Sigma13(1\bar{4}30)$ 27.80°, $\Sigma19(3\bar{5}20)$13.17°, and $\Sigma31(1\bar{6}50)$17.90°. Additionally, we studied two twist GBs that also had rotation axes about $[0001]$, similarly denoted by: $\Sigma7(0001)$21.79° and $\Sigma13(0001)$27.80°.

All simulation cells (supercells) were simulated under full periodic boundary conditions. For each GB supercell, we constructed corresponding bulk and free surface supercells of approximately equivalent size and shape, enabling the calculation of the works of separation and surface energies, as discussed below. After construction, the atoms within a given supercell were relaxed, whilst fixing the supercell itself. The microscopic degrees of freedom of the GBs were adequately explored, in order to identify GB structures that were thermodynamically plausible. For the exchange correlation functional, we employed the Perdew, Burke and Ernzerhof variant of the generalised gradient approximation [28], which has been demonstrated to predict bulk and surface properties of metal with reasonable accuracy [29]. In all simulations, we used a plane wave cut-off energy of 360 eV, at which point total supercells energies were converged to within 0.01 eV/atom. Furthermore, k-points were sampled according to a Monkhorst-Pack (MP) grid [30]; we used a maximum k-point separation of 0.04 $Å^{-1}$, for which the grain boundary energy was found to be converged to within 0.02 J/m^2. To mitigate numerical instabilities associated with simulating metals, we used a Gaussian smearing of 0.1 eV to smooth the electronic occupancies around the Fermi level. Self-consistent field iterations were terminated upon reaching an energy change of 1e-7 eV/atom. Furthermore, geometry optimisation, for which we used the Broyden-Fletcher-Goldfarb-Shanno

algorithm [31], was terminated upon reaching a change in energy of 1e-6 eV/atom and an atomic force tolerance of 1e-2 eV/Å.

The ideal work of separation of a grain boundary or bulk material on a given plane, which gives an approximate measure of its resistance to cleavage, was calculated according to:

$$W_{\mathrm{GB/B}} = \frac{1}{2A}\left(2E_{\mathrm{FS}}^{\mathrm{tot}} - E_{\mathrm{GB/B}}^{\mathrm{tot}}\right),$$

where A is the interface area, $\mathrm{E}_{\mathrm{FS}}^{\mathrm{tot}}$ is the total energy of the free surface supercell after atomic relaxation, and $\mathrm{E}_{\mathrm{GB/B}}^{\mathrm{tot}}$ is the total energy of either the GB or bulk supercell after relaxation. The grain boundary or free surface energy can be computed according to:

$$E_{\mathrm{GB/FS}} = \frac{1}{2A}\left(E_{\mathrm{GB/FS}}^{\mathrm{tot}} - \frac{n_{\mathrm{GB/FS}}}{n_{\mathrm{B}}}E_{\mathrm{B}}^{\mathrm{tot}}\right),$$

where $n_{\mathrm{GB/FS}}$ is the number of atoms in the GB or free surface supercell, and n_{B} is the number of atoms in the bulk supercell, and other terms are as previously defined.

For a subset of the systems under investigation (the Σ7 and Σ13 systems – both STGB and twist GBs and their corresponding bulk systems), we also examined the effect on the work of separation of introducing a single substitutional iodine atom near the cleavage plane. In these cases, the defective work of separation was calculated according to:

$$W_{\mathrm{GB/B}}^{\mathrm{def}} = \frac{1}{2A}\left(E_{\mathrm{GB/B}}^{\mathrm{tot}} + 2\left(\mathrm{E}_{\mathrm{FS}}^{\mathrm{tot,def}} - \mathrm{E}_{\mathrm{GB/B}}^{\mathrm{tot,def}}\right)\right),$$

where $\mathrm{E}_{\mathrm{FS}}^{\mathrm{tot,def}}$ and $\mathrm{E}_{\mathrm{GB/B}}^{\mathrm{tot,def}}$ refer to the total energies of the *defective* free surface and GB/bulk supercells, respectively, which include the substitutional iodine defect.

Results

Direct current potential drop measurements

The DCPD curve for this test is shown in Figure 4 with each phase of the test numbered from 1 – 7. Phase 1 included prefatiguing at 0.1 Hz where the maximum and minimum loads were 3500 N and 500 N, respectively. In phase 2 a dwell of 600 seconds was added between fatiguing cycles. As expected, the crack growth rate dropped dramatically compared to phase 1. In phase 3 the only change was that cover gas was diverted through the iodine flask such that iodine entered the specimen chamber. The crack growth rate immediately increased suggesting that I-SCC was occurring (phase 4). In phase 5 the loading changed to constant load equivalent to K=20 MPa√m (load 3800 N) and a steady rapid crack growth rate was achieved. In phase 6, the crack temporarily slowed when the load was dropped from 3.8 kN to 2.5kN. Even when fresh iodine was no longer entering the chamber (phase 7) the crack continued to grow quickly until the test was stopped.

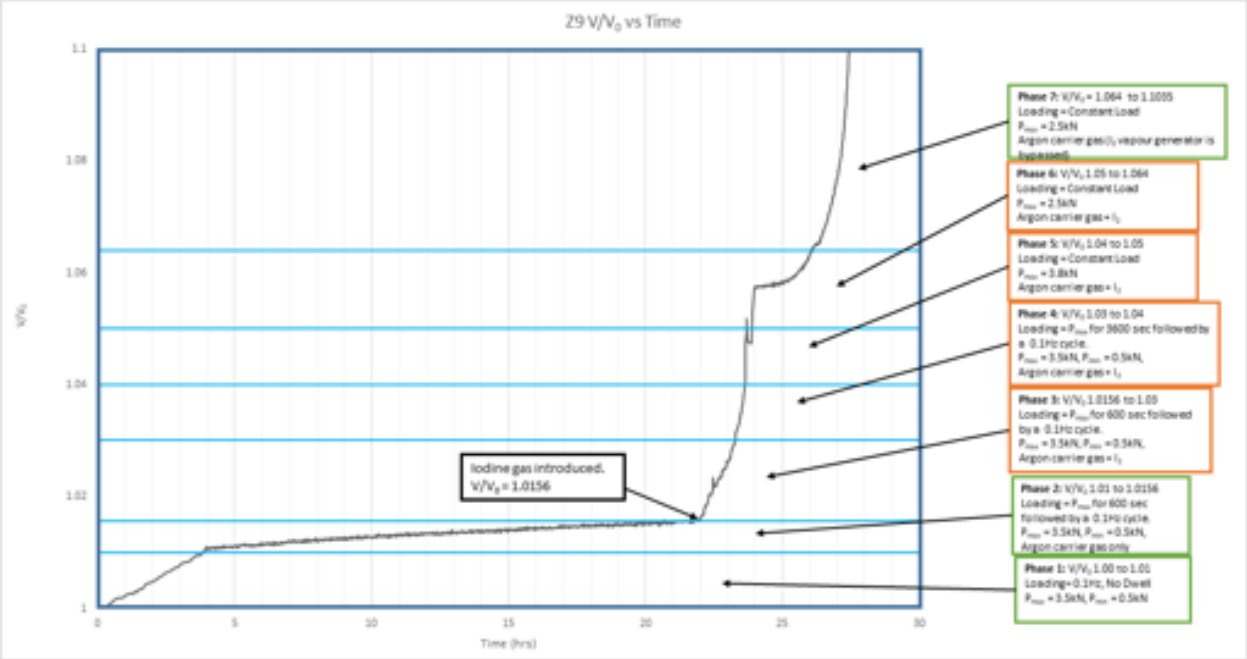

Figure 4: Direct current potential drop measurements for failed Zircaloy-4 CT specimen

3D microstructure and crack path

The reconstructed EBSD and crack path data is shown in Figure 5. The EBSD volume contains 959 grains, with an average grain diameter of 8.84 μm and average grain volume of 1260.49 μm^3. The 3D shape of the grains was assessed by fitting ellipsoids to the grains and extracting the ratio of the principal axes [32]. The average values of the b/a and c/a aspect ratios are 0.69 and 0.47 respectively, which indicates a surprisingly non-equiaxed microstructure when assessed in 3D. From the aligned datasets it was possible to analyse which grains were involved in the crack path and what type of cracking had occurred. 93 of the grains within the volume were observed to be involved in the crack path; 58 of these had cracked transgranularly (TG) and 35 were involved in intergranular (IG) cracking. The relative percentage of IG and TG cracking as a function of crack length is shown in Figure 6. It can be seen that the cracking is dominated by transgranular fracture throughout the volume. Towards the crack tip, the percentage of TG cracking is higher and more IG cracking is observed away from the crack tip as the crack widens through the volume. This is partly attributed to the break up of the recrystallised structure and the formation of subgrains ahead of the crack, which will be discussed in detail later. It appears that this intergranular cracking usually bridges small regions between larger TG grains, with minimal deviation from the original crack path.

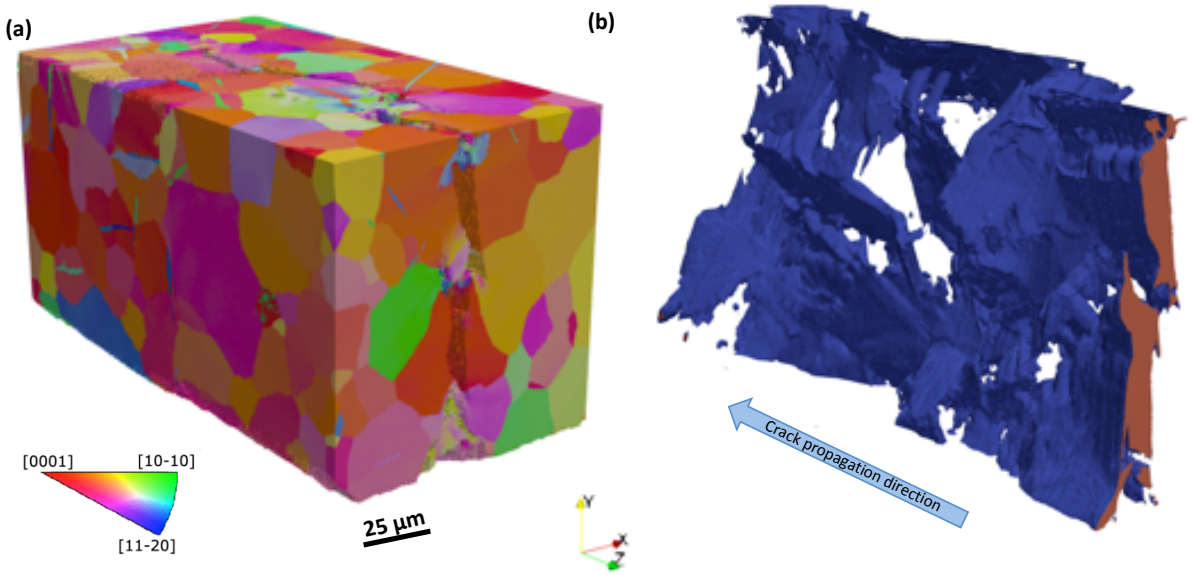

Figure 5: 3D reconstructions from serial sectioning experiment (a) EBSD data in IPF-X colouring and (b) FSD data showing crack path

The segmented crack, shown in Figure 5 (b), was entirely interconnected with a total volume of 42487 μm^3 which is approximately ~2% of the total analysed volume. It can be seen that the crack significantly widens away from the crack tip. Figure 6 shows that the average crack width increases almost linearly with crack length. There is also a significant shape change as the crack progresses; towards the crack tip, the crack path is more tortuous and closely follows the recrystallised grain morphology, and as the crack widens it becomes more planar until it extends into almost a single vertical crack at the end of the volume furthest away from the crack tip. There are several crack branches that emanate away from the main crack path, particulary towards the crack tip.

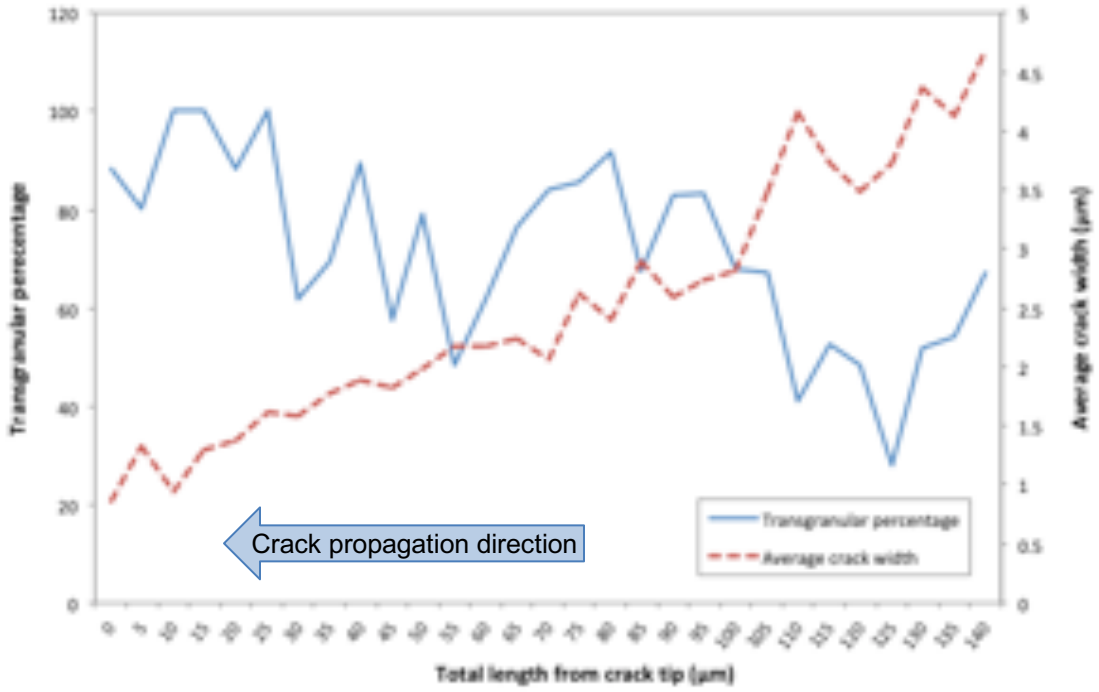

Figure 6: Percentage of transgranular cracking and average crack width as a function of total crack length

Orientation analysis

The orientations of all the voxels within a segmented grain were averaged and used to plot $\{10\bar{1}0\}$ and $\{0001\}$ pole figures. Pole figures for all 959 grains in the dataset are shown in Figure 7 (a). The pole figures are presented as raw data from the original sample normal direction (ND) and are coloured in IPF-X colouring in order to be consistent with previously presented orientation maps. The X direction of the 3D volume is parallel to the original ND direction of the sheet material. The material shows the expected split basal texture that occurs during thermomechanical processing [33], with a split of the $\{0001\}$ poles in the transverse direction (TD) and preferential alignment of the $\{10\bar{1}0\}$ poles towards the rolling direction (RD), although this is difficult to see in the raw pole figure data, it can clearly be seen in the contoured pole figures (not shown here). The orientations of the grains that were observed to have cracked transgranularly are shown in Figure 7 (b). These grains are observed to be largely oriented with the $\{0001\}$ pole close to ND direction, however there does not appear to be any strong preferential orientation of the $\{10\bar{1}0\}$ prismatic planes. It should also be pointed out that there are a small percentage of grains orientated away from the $\{0001\}$ orientation, with the $\{10\bar{1}0\}$ more closely oriented towards ND. A greater spread of orientations is observed in those grains involved in intergranular cracking, Figure 7 (c). It is also noted that of the 35 grains involved in IG, 15 of these were also involved in TG cracking.

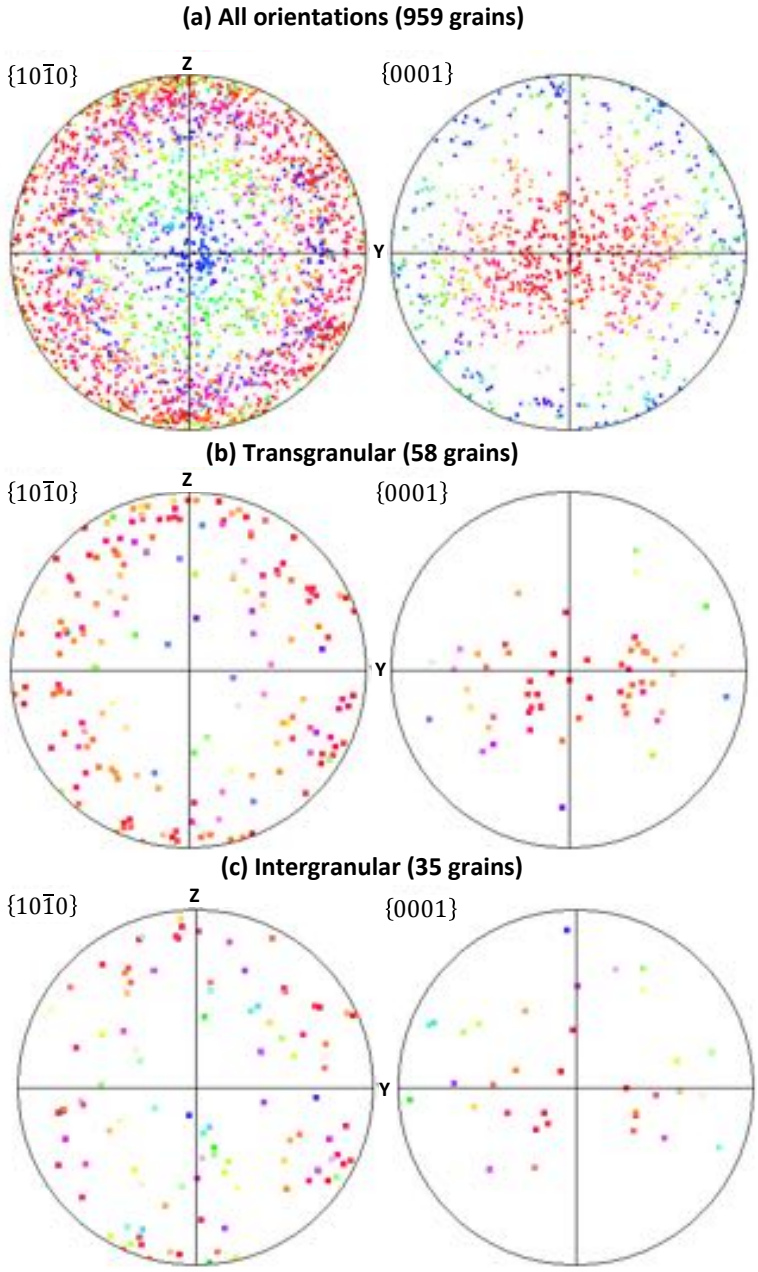

Figure 7: $\{10\bar{1}0\}$ *and* $\{0001\}$ *pole figures showing (a) all grains in volume (b) those grains that have cracked transgranularly and (c) those that were involved in intergranular cracking. The average orientation of all voxels in each grain is plotted and coloured according to IPF-ND colouring in order to be consistent with orientation maps.*

For those grains that have exhibited transgranular failure, the deviation of the cracking angle from the trace of the basal plane was calculated. A histogram of these deviations is shown in Figure 8 (a) and clearly demonstrates that the large majority of the transgranular cracks are within 20° of the basal plane of the grain through which they propagate. For those grains that have exhibited intergranular failure, the average orientations have been used to calculate the misorientation across the failed grain boundary. The relative frequency of these grain boundary misorientations is plotted in Figure 8 along with the misorientation angle distribution for the entire dataset. Although these results should be taken with

caution due to the small sampling volume, there are some obvious differences between the two distributions. The most significant difference is that no intergranular cracks were observed in the most common type of boundaries in the dataset, with misorientation of ~85°. These are most likely to be twin boundaries and will be discussed in more detail later.

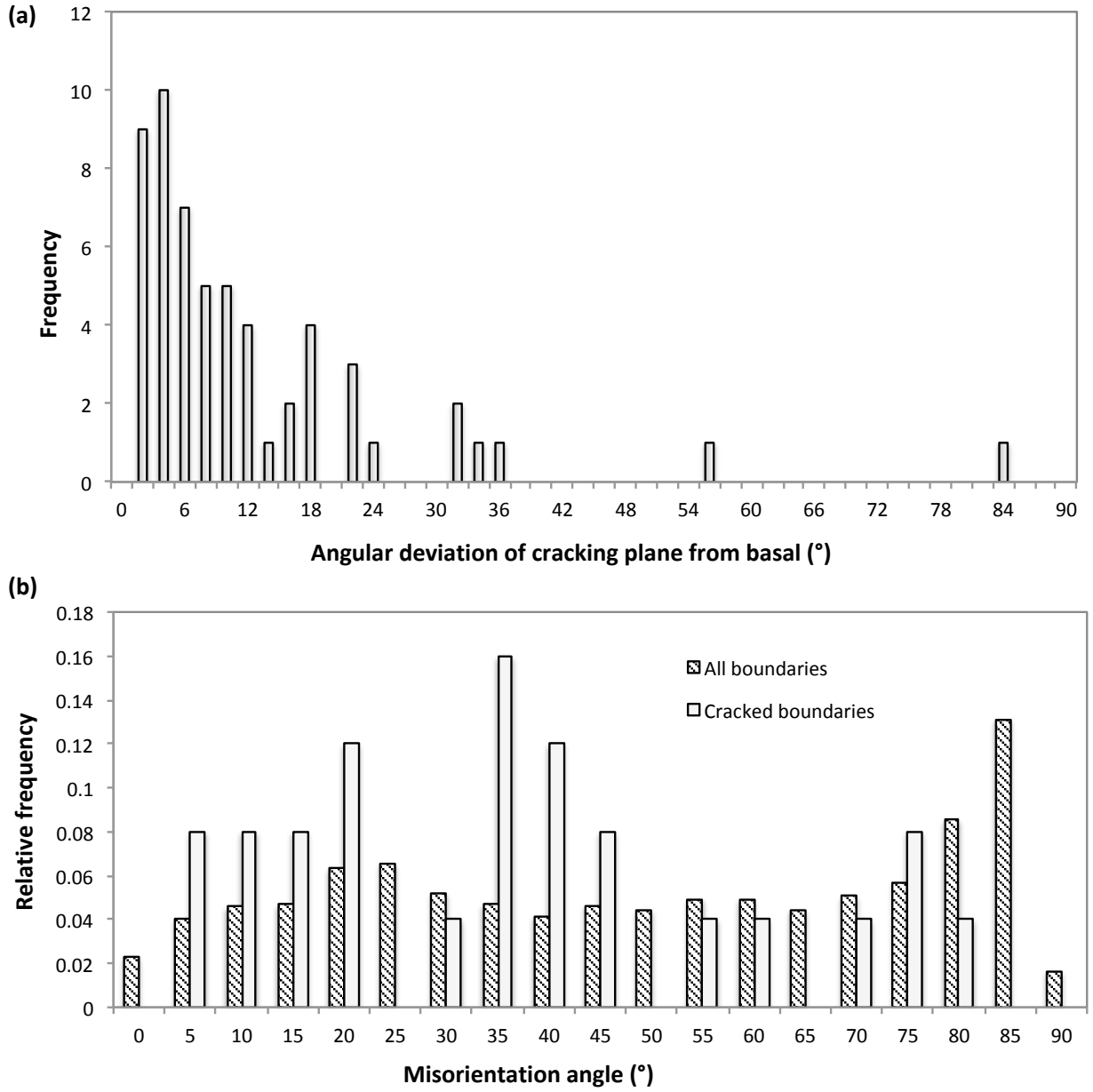

Figure 8: Angular dependence of transgranular and intergranular cracking (a) Frequency of angular deviation of transgranular cracking plane from (0001) basal plane and (b) Misorientation angle distribution of all grain boundaries within dataset (dashed) and boundaries subject to intergranular failure (white). Frequency plotted relative to all boundaries and only to cracked boundaries respectively.

Deformation surrounding crack tip

The misorientation within the grains was quantified by calculating the misorientation of each voxel within a grain with respect to average orientation, each grain is then assigned a 'feature average misorientation' which is an average of all the misorientation values within a particular grain. Grains can then be coloured according to this average intragranular misorientation value, which indicates the extent of deformation within the 3D volume, as shown in Figure 9 (a). Qualitatively it can be seen that grains in the immediate vicinity of the crack path exhibit significant higher levels of misorientation than the surrounding grains. In particular, grains that appear to bridge between different crack branches show the highest levels of misorientation, these will be discussed in more detail later. A comparison of the frequency of these intragranular misorientations between different types of grains is presented in Figure 9 (b). The frequency of bulk grains, i.e. those not involved with cracking, follows the expected trend for a recrystallised material, with the large majority of grains with less than 2° average misorientation. For those grains involved with intergranular cracking, it can be seen that the distribution is shifted towards higher average misorientation values, with the majority between 1 and 3°. For grains that have cracked transgranularly, the distribution is shifted again towards higher misorientation values, with the majority of grains having average intragranular misorientations between 2 and 4°. Also shown are grains that were in the crack path but were observed to significantly deflect the crack path, this group of grains showed the highest intragranular misorientation with the majority between 5 and 6°. At the higher end of the scale, it can be seen there are far less grains in the bulk with large misorientations greater than 8°, but these are relatively common in the grains in the vicinity of the crack path.

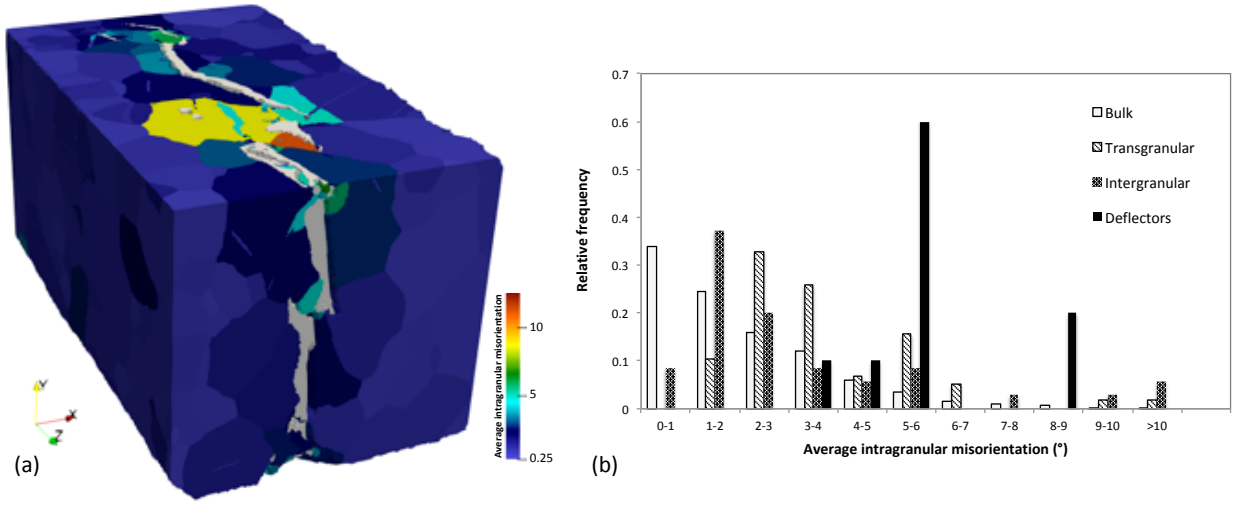

Figure 9: Quantification of deformation surrounding crack path, (a) 3D reconstruction of crack (white) with grains coloured according to average intragranular misorientation, (b) Comparison of relative frequencies of average intragranular misorientation for those grains in the bulk (white), those involved in transgranular cracking (striped),those involved in intergranular cracking (patterned) and those grains that deflected the crack (solid).

Another interesting observation is the occurrence of twins in the vicinity of the crack in comparison to the bulk. Figure 10 (a) shows an example XY slice through the 3D volume approximately 85 µm from the crack tip in IPF-ND colouring. Extensive twinning can be observed close to the crack that is much less prevalent in the bulk grains away from the crack path. In an attempt to quantify this twin formation, the numbers of twins close to the crack and in the bulk were counted at 5 µm intervals throughout the entire volume and are plotted in Figure 10 (b). Close to the crack is defined as within one grain width of the crack path in this case. It can be seen that throughout the volume, the number of twins close to the crack is greater than in the bulk. Furthest away from the crack tip where the crack is widest (see Figure 6), it can be seen that the number of twins both in the bulk and close to the crack is relatively low. As the crack narrows, the number of twins close to the crack increases significantly and reaches a maximum approximately 90 µm from the crack tip. In this region there is also a significant amount of grain break up, an example of which can be seen in Figure 10 (a) which is associated with a ligament between two crack branches and will be discussed in more detail later.

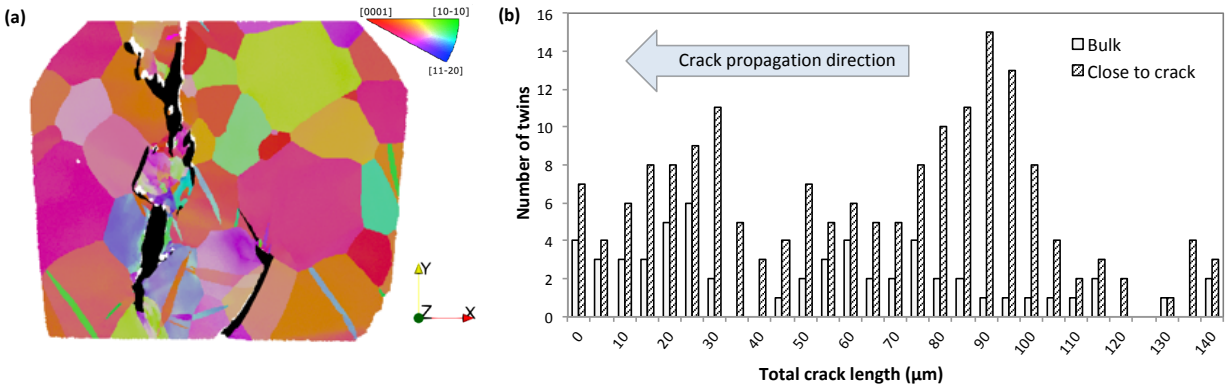

Figure 10: Effect of crack path of twin formation, (a) Selected XY slice through 3D volume in IPF-X colouring showing high twin fraction and grain breakup close to crack path, (b) Comparison of number of twins in bulk grains to those close to crack (defined as within one grain of crack path) as a function of crack length.

Deviations in crack path

As well as investigating the grains and boundaries through which the crack propagates, it is also of interest to investigate those grains that were in the crack path but did not crack. The grains that deflected the crack were identified by virtually slicing the 3D dataset in the XZ plane so that the direction of crack propagation could clearly be seen. Grains were then manually identified from these 2D slices and then the deviation was confirmed in 3D by superimposing the 3D crack path over the 3D grain structure. An example of this procedure is shown in Figure 11 (a) – (c). In total 10 grains of these 'deflector' grains were identified, the orientations of which are plotted on pole figures in Figure 11 (d). The pole figures show a tendency towards non-basal orientation in these grains, and particular grains with the {0001} poles aligned towards the TD direction. These grains also show extremely high levels of intragranular misorientation compared to the bulk grains, as shown in Figure 9(b).

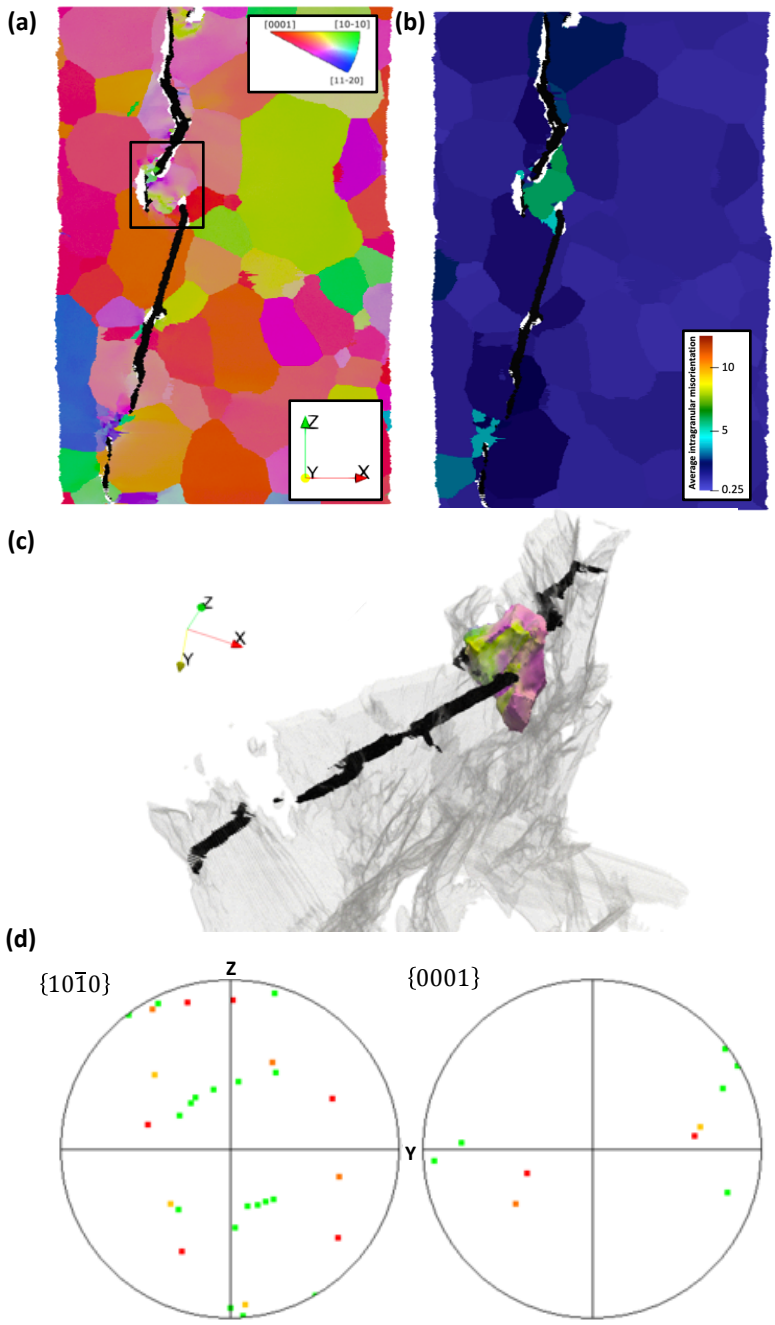

Figure 11: Identification and orientation of grains within the volume that deflect the crack path, (a) XZ slice in IPF-ND colouring showing region of crack deflection, (b) XZ slice coloured according to average intragranular misorientation showing high levels of deformation in this region, (c) 3D grain in IPF-X colouring overlaid with XZ slice through segmented crack data and full 3D reconstructed crack path confirming that crack deviated around grain in 3D, (d) $\{10\bar{1}0\}$ *and* $\{0001\}$ *pole figures showing average orientation of all 10 grains that deflected the crack.*

Simulated interface energetics by DFT

In Figure 12, we show both the pristine and defective works of separation for the Σ7 and Σ13 symmetric tilt and twist GBs. We note that the effective strengths of the GBs vary according to the GB type and plane. The GB that has the largest pristine work of separation, and so, in approximate terms, is the most resistant to fracture, is the Σ13 STGB. On the other hand, the Σ7 STGB has the lowest pristine work of separation. The pristine works of separation of the twist GBs are very similar. Across all GBs, there is a clear lowering of W_{GB} due to the presence of the iodine substitutional defect at the interface. This implies iodine has an embrittling effect on the GBs as a result of reducing their cohesion.

Defect areal concentrations are also indicated in Figure 12. Due to differences in the size and shape of each periodic supercell, the replacement of a host Zr atom with a single iodine atom represents a different defect concentration in each supercell. For instance, the highest defect areal concentration is for the Σ7 STGB, since the area of the interface plane in this supercell is the smallest. We therefore opted to also calculate normalised defective works of separation. As can be seen in Figure 12, we chose as the nominal concentration that of the iodine defect in the Σ13 twist GB, which had the largest interfacial area and so the smallest defect concentration. Due to the system-size restriction associated with first-principles calculations (DFT calculations are computationally expensive and scale with the cube of the number of atoms), all of defect concentrations that we probed are relatively high (since the supercells are periodic). Therefore, we chose the smallest concentration as the nominal value for normalisation. The normalisation was done by interpolating (for each system with higher concentrations) the value of W_{GB} at the nominal concentration level. For this to be valid, it is necessary that the work of separation changes linearly with the defect concentration. We investigated this by considering the effects of adding further substitutional defects to both the Σ7 STGB and Σ7 twist GB, and their associated bulk systems. It was found that the relationship between the work of separation and the defect concentration for zero to two defects is approximately linear. Upon the addition of a third defect, the relationship deviated from linearity. However, for our purposes, this is satisfactory, because, for all systems, our chosen nominal concentration is situated between the concentrations of zero and one defect.

Considering the normalised values of W_{GB} in Figure 12, we see that the defective values for both the twist GBs and the Σ13 STGB are quite similar, despite the slightly larger variance exhibited by the pristine works of separation for these systems. The (normalised) defective work of separation of the Σ7 STGB is smaller than that of the other systems; however, the pristine value is also considerably smaller. In summary, all studied GBs are embrittled by iodine, and given a consistent iodine concentration, the defective work of separation of the Σ7 STGB is the lowest, and hence more likely to cleave.

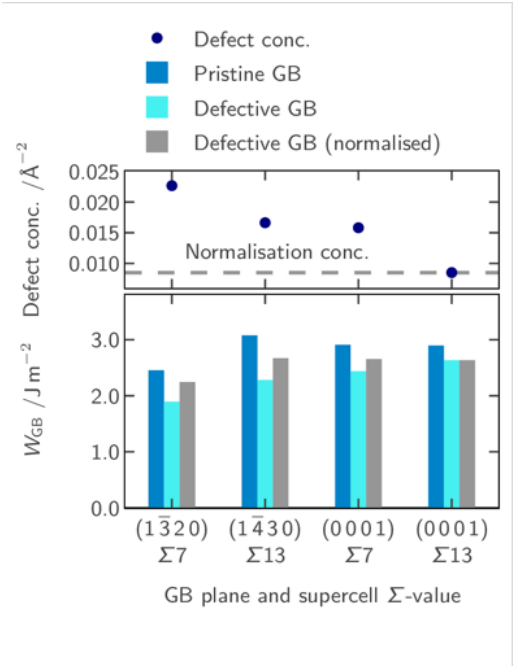

Figure 12: The effect of iodine on the work of separation for two symmetric tilt GBs and two twist GBs in Zr. The third bar for each system indicates the effective work of separation as normalised according to the areal defect concentration in the Σ13 twist GB.

We performed a similar analysis on the equivalent bulk systems, as portrayed in Figure 13. We can firstly note that the pristine works of separation of all bulk systems are larger than those of the GBs. From this, we can infer that it is more difficult to cleave a given plane in the bulk than in a GB, which is to be expected, since GBs represent areal defects, for which the atomic bonding is perturbed. Additionally, we found the pristine works of separation for cleavage on the basal planes to be lower than that on the non-basal planes, i.e. the pristine basal planes appear to be easier to cleave.

As in the case of the GBs, inserting iodine near to the cleavage plane results in a lowering of the work of separation, W_B. The magnitude of this lowering is most substantial for the $\Sigma13(1\bar{3}20)$ system (where we now use the Σ-value in reference to the corresponding GB system, and to signify the Σ-value of the supercell). We see that, whereas for the pristine systems, the basal planes are weaker, for the defective systems, the non-basal planes become weaker. However, considering the effect of the normalised concentrations in Figure 13, the basal planes are once again the weakest planes.

We used our DFT-calculated surface energies to investigate how the crack path might propagate with energetic preference across given crystallographic planes. The surface energies for each of the studied systems are shown in Table 1. The basal plane from the Σ13 supercell is not included, since, this surface is physical identical to that from the Σ7 supercell. We see that the surface energy of the basal plane is particularly small, relative to that of the prismatic planes, which helps to explain why the pristine works of separation at the bulk basal planes are smaller than those at the non-basal planes.

Table 1: Surface energies of four prismatic planes and the basal plane in Zr, computed using DFT.

$\boldsymbol{\Sigma}$	Interface	Surface energy, $\boldsymbol{E_{FS}}$ / J/m^2
7	$(1\bar{3}20)$	1.70
13	$(1\bar{4}30)$	1.79
19	$(3\bar{5}20)$	1.69
31	$(1\bar{6}50)$	1.76
7	(0001)	1.59

From the Griffith criterion for brittle fracture [34], we note that, under the approximations of elastic isotropy and fast brittle fracture, the critical stress for crack growth, σ_c, is proportional to the square root of the surface energy: $\sigma_c \propto \sqrt{E_{FS}}$. In Figure 14, we schematically illustrate how we can use this relationship to predict which planes are energetically accessible to a propagating crack. Consider a plane whose normal is perfectly aligned with the loading direction, such that crack propagation would result in cleavage of that plane (as shown in purple on the left in Figure 14). If this perfectly aligned plane is one whose critical stress is larger than some other alternative plane (shown in green on the right in Figure 14), then cleavage may occur on the alternative plane, even if it is misaligned in such a way that its normal direction does not coincide with the loading direction. In other words, if we consider loading the perfectly aligned plane to its critical fracture stress, we can resolve this stress in the direction of the misaligned plane normal, and for misalignment within some threshold angle, ϕ, the resolved stress would be sufficient to cleave the alternative plane. In Figure 14, we demonstrate what these misorientation angles are, given the $(1\bar{4}30)$ plane is perfectly aligned with the loading direction.

In Figure 15, the misorientation angles, ϕ, for each perfectly aligned plane are shown. For example, the blue crosses represent the situation where the plane that is hardest to cleave, the $(1\bar{4}30)$ plane (which has the largest surface energy and so the largest critical fracture stress, given our aforementioned approximations) is perfectly aligned for cleavage. In this case, each of the other studied surfaces may be an alternative cleavage path for the crack (if the alternative plane is within a threshold misalignment, ϕ) since the largest critical fracture stress can be resolved onto each of the misaligned directions. For the plane with the next-largest critical fracture stress, only three of the remaining planes are energetically accessible, and so on. Our results demonstrate that there can exist a relatively large misorientation away from perfect alignment, and cleavage may still occur on non-aligned planes. For example, we can see in Figure 15 that the bulk basal plane can be misaligned away from the loading direction by up to (approximately) 15 to 20 degrees, and basal cleavage would be equally likely to cleavage on any of the other prismatic planes. The result supports our experimental observations that cleavage occurs primarily on transgranular basal planes. Given the measured texture, many basal planes with this alignment are likely to exist. Furthermore, we note that, although from considering Figure 12 and Figure 13 we can see that the defective twist GBs have a lower work of separation than the equivalent defective bulk basal planes, since this difference is quite small, it is reasonable to interpret this, in light of the experimental results, to mean that it is not energetically favourable for the crack to "seek out" the basal GBs. It is instead more favourable for the crack to propagate along a slightly misaligned bulk basal plane.

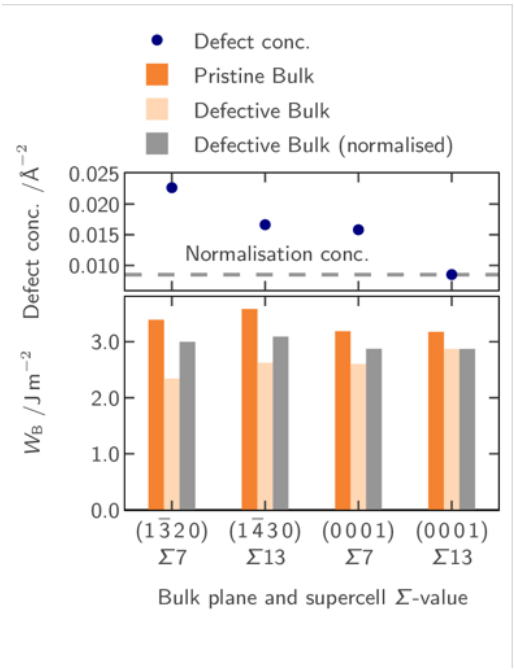

Figure 13: The effect of iodine on the work of separation for the set of bulk systems that correspond to the GB systems referred to in Figure 1. Each bulk system was cleaved at a plane equivalent to the GB plane as described in the basis of one of the crystals in the corresponding GB system.

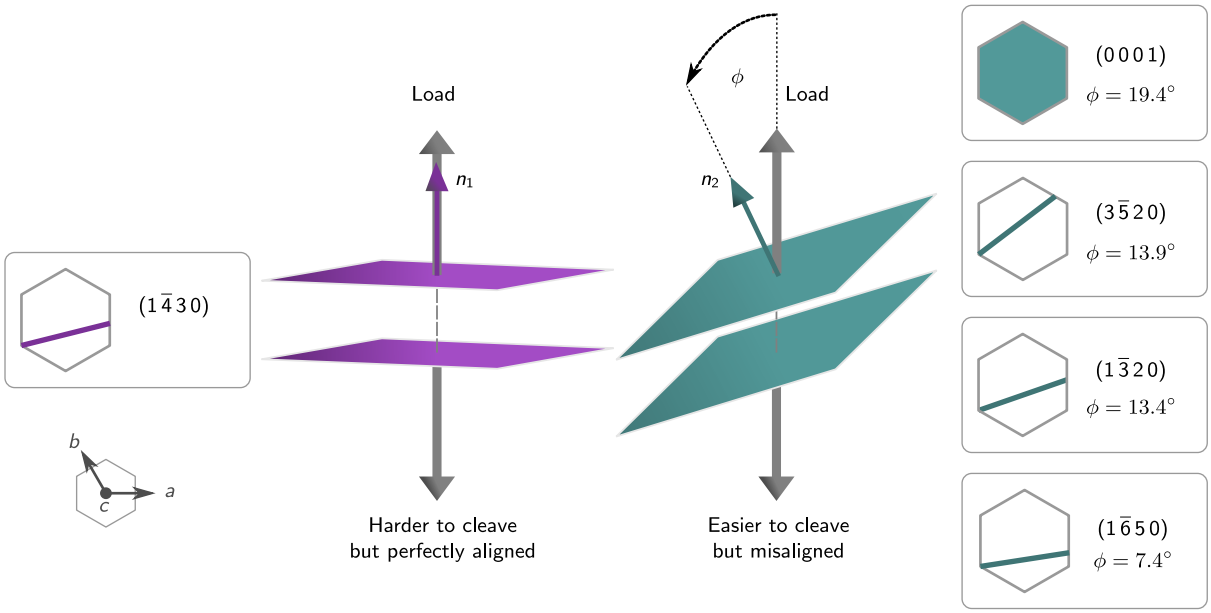

Figure 14: Schematic representation of possible cleavage planes. For a given plane that is more difficult to cleave but perfectly aligned with respect to the crack path (left), cleavage may occur on planes that are easier to cleave but misaligned (right), if the misalignment is within some threshold angle, ϕ.

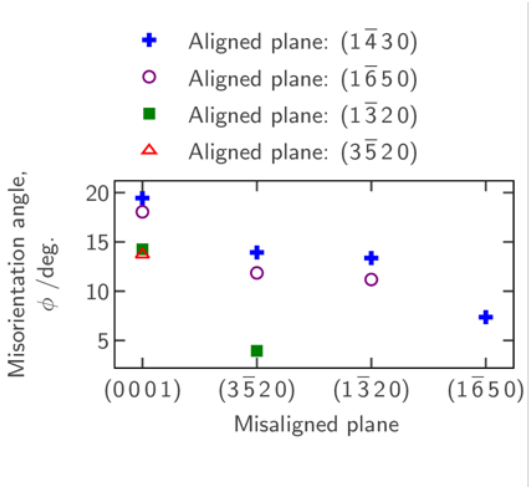

Figure 15: For a given plane that is perfectly aligned with respect to the crack path, other misaligned planes may cleave if the misalignment is within an angle ϕ. The blue crosses represent the scenario depicted in the schematic of Figure 14, where the $(1\bar{4}30)$ *plane (which had the largest critical fracture stress) is perfectly aligned for cleavage.*

Discussion

The careful control and monitoring of the crack progression by DCPD measurements enabled by the testing method used allowed a crack to be arrested and studied in great detail. This was vital for the investigation as detailed characterisation of the crack path can then be combined with atomistic scale simulations provides novel insights into the likely mechanisms that dominate its propagation.

3D microstructure and crack path

The analysis of the three-dimensional EBSD data shown in Figure 5 demonstrates the value of not just considering a typical two-dimensional slice when examining complex crack propagation with respect to local microstructure. Visualizing the full extent of the crack in direct correlation the surrounding grain morphology and crystallographic orientations of adjacent grains allows much more significant insights to be made about the progression of the crack and the implied failure mechanisms. Simpler 2D analyses carried out previously may not only miss important features but also lack the statistics to make confident conclusions about the mechanisms observed. The large number of grains assessed in 3D also allows quantification of the underlying microstructure, showing that grains were less equiaxed in morphology that might be expected. In this case, no particular correlation was found between the grain shapes and the crack paths, but for more complex microstructures such as those found in partially recrystallised or stress relieved materials, a grain morphology effect may be more significant in terms of crack propagation and could be assessed using the current method.

The segmented crack surface shown in Figure 5b demonstrates a variation of the crack plane with features that appear to be similar to microstructural features, this surface would be similar to what would be observed on by fractography. The ability to observe the crack surface in direct correlation to the

microstructure allowed the classification of the crack as IG or TG with respect to each grain it intersected. Overall, it appears that TG cracking was the dominant mode, which may be related to the crystallographic texture of the material relative to the crack path (discussed later), however it is also evident more IG cracks are observed in the earlier part of the crack where the shorter crack length may be associated with a lower stress intensity. The smaller intergranular cracks are often interspersed between regions of TG crack and these may related to features often characterized as fluting in fractography analysis of I-SCC specimen [20].

Orientation of cracks relative to microstructure

It should be noted that the samples chosen for this analysis was manufactured such that the direction of the applied load (X) was parallel to the original ND direction of the plate. As illustrated in Figure 7a this resulted in a large proportion of the grains oriented with their basal planes oriented close to the direction of crack propagation (Z). As basal plane cleavage has been reported as a preferred route of fracture during I-SCC, it is therefore not surprising that a high proportion of TG cracking is observed. Indeed when analyzing the TG crack plane relative to the basal plane orientation, Figure 8a, a clear correlation is observed, confirming that most TG cracking occurred along the basal plane. This also agrees well with the results from DFT simulations shown in Figure 13 which (for the limited planes assessed) suggest that, for a given concentration of iodine, cleavage along the basal plane would be easiest and that basal cleavage may be preferred even when basal planes are oriented up ~20° from the nominal crack direction (see Figure 14 & Figure 15).

Despite the strong texture, a significant number of grains that interacted with the crack were of an orientation where their basal planes where not suitably oriented for the crack to propagate easily. In these instances the crack was observed to deviate towards the basal plane (Figure 7b) or propagate by IG cracking. Figure 7c shows the orientation of grains at which IG was preferred and demonstrates a much greater spread. With regards to preferential grain boundaries for crack propagation, things become more complex. Figure 8b suggests that there may indeed be some preference of IG along certain boundaries as the distribution of cracked boundaries is different to the overall distribution. The boundaries most commonly observed to IG cracking (~35°) are not the most common in the microstructure, similarly no boundaries with 85° misorientation were observed to show IG despite these being the most common type of boundary in the microstructure. Interestingly, of the boundaries studied by DFT the lowest work of separation was observed for the $\Sigma 7(1\bar{3}20)$ boundary, which has a misorientation angle of 21.79°, which is matches one of the most frequently experimentally observed cracked boundaries (Figure 8b). The less susceptible non-basal boundary according to DFT, $\Sigma 13(1\bar{4}30)$, represents a misorientation of 27.80°. Experimental observations show a much lower proportion of cracked boundaries close to this misorientation (Figure 8b).

However, care must be taken when comparing grain boundaries as they are very complex features, which require essentially five parameters to fully describe them [35]. DFT modelling has shown that misorientation is not a good indication of GB energy [36] and therefore its propensity for defect accumulation as well as cleavage. Indeed, the plane of the boundary is not considered when using average misorientation and this may have an equal if not more significant effect. The capture of 3D

microstructures shown here, does allow for grain boundary planes to be assessed, and this complex analysis will be pursued in future work.

Despite the difficulties in assessing grain boundary character, simulations can shed some light on the determination of the crack path. As for bulk planes, iodine is shown to lower the work of separation for all the boundaries studied, thereby enhancing crack propagation. This suggests that iodine induced intergranular cracking is indeed energetically feasible. For the limited boundaries assessed, the simulations in fact suggest that GBs should be more susceptible than bulk planes (see Figure 12 & Figure 13), although the difference is small. The experimental observations show a clear preference for TG cracking along bulk planes, although as mentioned earlier the fraction of IG observed is higher earlier in the crack progression. It is likely that kinetics may play an important role in determining, where in the earlier stages of cracking iodine has enough time embrittle to boundaries, but as the stress intensity increases IG cracking is preferred. This correlation has recently been observed for I-SCC tests carried out in alcoholic solution [12] .

Looking at misorientations within grains can be a useful indication of the deformation experienced by individual grains as the crack progresses, which can be used to assess the grain's resistance to I-SCC, i.e. the stress experienced before a crack progresses. Interestingly, the grains adjacent to IG cracks show the lowest evidence of deformation (see in Figure 9b), suggesting again that when local stress is lower IG cracking may be more likely. Conversely, grains where TG cracks are observed, show higher levels of deformation, suggesting they experienced higher local stresses which may have enhanced IG cracking. These observations provide strong evidence at a microstructural level to support the previously suggested relationship between stress intensity and the nature of crack propagation [1,2,8,12].

Grains where the crack was seen to deflect, showed evidence of high deformation (see Figure 11), which suggest that stress was not the limiting factor for their failure by I-SCC, but rather a lack of iodine or a particular resistance to its attack. These grains were shown to have a tendency towards non-basal orientations with most also showing alignment of {0001} poles the direction of crack propagation.

Twinning is also an indication of the local stress in the microstructure and Figure 10 demonstrates that significantly higher levels of twin formation is observed in the vicinity of the crack, especially as it progresses. Twins that form in grains near to a progressing crack may be expected impact crack progression in two main ways. Firstly the formation of the twin may relieve the stress in the affected grain making it less likely to undergo TG cracking, meaning the crack will take an alternative path. Secondly, where a grain does undergo TG, a twin within it may deflect the crack as the basal planes will no longer be available to the crack when it reaches the twin. Both these features were observed in the volume analyzed and combined with the lack of IG cracking on typical twin boundaries (i.e. GBs with 85° misorientation) points to a potential benefit provided by twinning in the microstructure.

Overall this work highlights the potential of using instrumented tests in combination with high-resolution 3D characterization techniques to relate crack propagation to the local microstructure providing new insights into I-SCC mechanisms. The resolution available also opens the opportunity to directly relate experimental observations to atomistic scale simulations which can probe the interaction of a range of fission product impurities with different microstructural features. Further development of the analysis

tools and their application to a range of microstructures and alloy chemistries are expected to make even more use of these capabilities.

Conclusions

Instrumented I-SCC tests using a newly developed facility has allowed cracked specimen to be produced under highly controlled conditions. Arrested cracks were characterized and related to their surrounding microstructure by detailed 3D EBSD analysis. Complementary first-principles simulations using density functional theory were used to assess the energetics of various Zr interfaces in the presence of iodine.

- Three-dimensional analysis is shown to be essential for full characterization of a crack with relation to microstructural features. With 3D EBSD providing statistically significant volumes of data to describe I-SCC crack progression, the nature and crystallographic orientation of the crack plane.
- For the sample studied transgranular (TG) cracking by basal cleavage was observed to be the most common path for the I-SCC crack, especially near to the arrested crack tip. However, significant levels of intergranular (IG) cracking (up to ~ 50%) were observed in the earlier regions of the crack.
- Most TG cracked grains were shown to be oriented with their basal planes near to the crack propagation direction and the vast majority of TG crack planes were within 10° of basal plane of the grain. Simulations suggested that TG basal cleavage is energetically accessible and may be preferable to cleavage on prismatic planes, even if this would result in the crack path deviating by up to 20°.
- IG cracks showed some preferential misorientations, but further study is required to quantify this relationship, due to the complex nature of grain boundaries. Simulations suggested that iodine should enhance IG cracking on all the boundaries studied.
- Correlation between misorientation within grains and the crack path suggest that higher stress intensity favours TG cracking.
- Grains with particular orientations and the formation of twins are shown deflect the crack during I-SCC and may have an important potential impact on crack propagation.

Acknowledgements

This work was funded by the EPSRC - PACIFIC [EP/L018616/1] Programme and is supported by EPSRC Centre for Doctoral Training in Nuclear Fission- Next Generation Nuclear [EP/L015390/1]. It has been carried out as part of the PACE consortium on Pellet Cladding Interaction

References

[1] B. Cox, Pellet-clad interaction (PCI) failures of zirconium alloy fuel cladding—a review, J. Nucl. Mater. 172 (1990) 249–292. http://www.sciencedirect.com/science/article/pii/002231159090282R (accessed July 22, 2013).

[2] M.H.A. Piro, D. Sunderland, S. Livingstone, J. Sercombe, W. Revie, A. Quastel, K. Terrani, C. Judge, A Review of Pellet–Clad Interaction Behavior in Zirconium Alloy Fuel Cladding, 2017. doi:10.1016/B978-0-12-803581-8.09799-X.

[3] G.A. Ferrier, M. Farahani, P.K. Chan, E.C. Corcoran, Mitigating the iodine-induced stress corrosion cracking of Zircaloy-4 fuel sheathing using siloxane coatings, in: Iodine-Induced Stress Corros. Crack. Work., 2015.

[4] S. Béguin, PCI-related Constraints on EDF PWRs and Associated Challenges, in: Organ. Econ. Co-Operation Dev. - Nucl. Energy Agency, 75 - Paris (France); 548 p; ISBN 92-64-01157-9; Worldcat; Jul 2005; p. 53-62; Semin. Pellet-Clad Interact. Water React. Fuels; Aix-En-Provence (France); 9-11 Mar 2004;, 2005: p. 53.

[5] S. Beguin, PCI-related constraints on EDF PWRs and associated challenges, in: Pellet-Clad Interact. Water React. Fuels, Organisation for Economic Co-Operation and Development - Nuclear Energy Agency, 75 - Paris (France); 548 p; ISBN 92-64-01157-9; Worldcat; Jul 2005; p. 53-62; Seminar: Pellet-clad Interaction in Water Reactor Fuels; Aix-en-Provence (France); 9-11 Mar 2004;, 2005: pp. 53–62.

[6] D. Rozzia, A. Del Nevo, M. Adorni, F. D'Auria, Modeling of BWR Inter-Ramp Project experiments by means of TRANSURANUS code, Ann. Nucl. Energy. 50 (2012) 238–250. doi:10.1016/j.anucene.2012.07.016.

[7] M.L. Rossi, C.D. Taylor, First-principles insights into the nature of zirconium–iodine interactions and the initiation of iodine-induced stress–corrosion cracking, J. Nucl. Mater. 458 (2015) 1–10. doi:10.1016/j.jnucmat.2014.11.114.

[8] S.Y. Park, J.H. Kim, B.K. Choi, Y.H. Jeong, Crack initiation and propagation behavior of zirconium cladding under an environment of iodine-induced stress corrosion, Met. Mater. Int. 13 (2007) 155–163. doi:10.1007/BF03027567.

[9] C. Gillen, A. Garner, P. Tejland, P. Frankel, High resolution crystallographic and chemical characterisation of iodine induced stress corrosion crack tips formed in irradiated and non-irradiated zirconium alloys, J. Nucl. Mater. (2019).

[10] J.R. Galvele, Surface mobility mechanism of stress-corrosion cracking, Corros. Sci. 35 (1993) 419–434. doi:10.1016/0010-938X(93)90175-G.

[11] S.B. Farina, G.S. Duffó, J.R. Galvele, Stress Corrosion Cracking of Zirconium and Zircaloy-4 in Iodine-Alcoholic Solutions, Corrosion. 59 (2003) 436–442. doi:10.5006/1.3277575.

[12] C. Gillen, A. Garner, P. Frankel, Investigating Iodine-Induced Stress Corrosion Cracking Of Zirconium Alloys Using Quantitative Fractography, Manuscr. Prep. (n.d.).

[13] C. Gillen, A. Garner, P. Tejlan, P. Frankel, High resolution crystallographic and chemical characterisation of iodine induced stress corrosion crack tips formed during laboratory testing of irradiated and non-irradiated zirconium alloys, Unpublished. (n.d.).

[14] K. Une, Deformation and Fracture Behavior of Zircaloy-2 Deformed at Constant Strain Rate in Iodine Environment, (I), J. Nucl. Sci. Technol. 16 (1979) 577–587. doi:10.1080/18811248.1979.9730949.

[15] K. Une, K. Nogita, S. Ishimoto, K. Ogata, Crystallography of Zirconium Hydrides in Recrystallized Zircaloy-2 Fuel Cladding by Electron Backscatter Diffraction, J. Nucl. Sci. Technol. 41 (2004) 731–740. doi:10.1080/18811248.2004.9715540.

[16] M. Peehs, H. Stehle, E. Steinberg, Out-of-Pile Testing of Iodine Stress Corrosion Cracking In ZIrcaloy Tubing in Relation to the Pellet-Cladding Interaction Phenomenon, in: Zircon. Nucl. Ind. 4th Int. Symp. ASTM STP 1132, 1979: pp. 244–260.

[17] R. Haddad, A. Dorado, Grain-by-grain study of the mechanisms of crack propagation during iodine stress corrosion cracking of Zircaloy-4, Zircon. Nucl. Ind. Tenth …. (1994).

[18] D.B. Knorr, J.M. Peltier, R.M. Pelloux, Influence of Crystallographic Texture and Test Temperature on Initiation and Propagation of Iodine Stress-Corrosion Cracks in Zircaloy, in: Zircon. Nucl. Ind. Sixth Int. Symp. ASTMSTP 824, 1982: pp. 627–652. doi:https://doi.org/10.1520/STP824-EB.

[19] A. Legris, C. Domain, Ab initio atomic-scale modelling of iodine effects on hcp zirconium, Philos. Mag. (2006).

[20] S.Y. Park, J.H. Kim, M.H. Lee, Y.H. Jeong, Stress-corrosion crack initiation and propagation behavior of Zircaloy-4 cladding under an iodine environment, J. Nucl. Mater. 372 (2008) 293–303.

doi:10.1016/j.jnucmat.2007.03.258.
[21] S. Hanlon, A. Phillíom, C. Gillen, M. Daymond, Development of a gaseous iodine testing system to determine the I-SCC properties of zirconium alloys, Submitt. to Environ. Degrad. (2019).
[22] C. Gillen, A. Garner, A. Plowman, C.P.C.P. Race, T. Lowe, C. Jones, K.L.K.L. Moore, P. Frankel, Advanced 3D characterisation of iodine induced stress corrosion cracks in zirconium alloys, Mater. Charact. 141 (2018) 348–361. doi:10.1016/j.matchar.2018.04.034.
[23] T.L. Burnett, R. Kelley, B. Winiarski, L. Contreras, M. Daly, A. Gholinia, M.G. Burke, P.J. Withers, Large volume serial section tomography by Xe Plasma FIB dual beam microscopy, Ultramicroscopy. 161 (2016) 119–129. doi:10.1016/j.ultramic.2015.11.001.
[24] M.A. Groeber, M.A. Jackson, DREAM.3D : A Digital Representation Environment for the Analysis of Microstructure in 3D, Integr. Mater. Manuf. Innov. 3 (2014) 1–17.
[25] P. Hohenberg, W. Kohn, Inhomogeneous Electron Gas, Phys. Rev. 136 (1964).
[26] W. Kohn, L.J. Sham, Self-Consistent Equations Including Exchange and Correlation Effects, Phys. Rev. 140 (1965).
[27] S.J. Clark, M.D.S. Ii, C.J.P. Ii, P.J.H. Iii, M.I.J.P. Iv, K.R. V, First principles methods using CASTEP, Z. Krist. 220 (2005) 567–570.
[28] J.P. Perdew, K. Burke, M. Ernzerhof, Generalized Gradient Approximation Made Simple, Phys. Rev. Lett. 77 (1996) 3865–3868.
[29] C. Fiolhais, L.M. Almeida, Surface Energies of Simple Metals from Slabs : Comparison of Exchange-Correlation Density Functionals, Int. J. Quantum Chem. 101 (2005) 645–650. doi:10.1002/qua.20321.
[30] H.J. Monkhorst, J.D. Pack, Special points for Brillonin-zone integrations, Phys. Rev. B. 13 (1976) 5188–5192.
[31] R.H. Byrd, J. Nocedal, R.B. Schnabel, Representations of quasi-Newton matrices and their use in limited memory methods, Math. Program. 63 (1994) 129–156.
[32] M. Groeber, S. Ghosh, M.D. Uchic, D.M. Dimiduk, A framework for automated analysis and simulation of 3D polycrystalline microstructures. Part 1: Statistical characterization, Acta Mater. 56 (2008) 1257–1273. doi:10.1016/j.actamat.2007.11.041.
[33] E. Tenckhoff, A Review of Texture and Texture Formation in Zircaloy Tubing, in: Zircon. Nucl. Ind. 5th Int. Symp. ASTM STP 754, 1982: pp. 5–25.
[34] A.A. Griffith, The Phenomena of Rupture and Flow in Solids, Philos. Trans. R. Soc. London. Ser. A, Contain. Pap. a Math. or Phys. Character. 221 (1921) 163–198.
[35] I. Ghamarian, P. Samimi, G.S. Rohrer, P.C. Collins, Determination of the five parameter grain boundary character distribution of nanocrystalline alpha-zirconium thin films using transmission electron microscopy, Acta Mater. 130 (2017) 164–176. doi:10.1016/j.actamat.2017.03.041.
[36] A.J. Plowman, Developing a mechanistic understanding of the pellet-cladding interaction with atomistic simulation, University of Manchester, 2018.